

Global simulation of plasma series resonance effect in radio frequency capacitively coupled Ar/O_2 plasma

Xue Bai(白雪), Hai-Wen Xu(徐海文), Chong-Biao Tian(田崇彪), Wan Dong(董婉), Yuan-Hong Song(宋远红), and You-Nian Wang(王友年)

Citation: Chin. Phys. B, 2023, 32 (**12**): 125203. DOI: 10.1088/1674-1056/ace427
Journal homepage: http://cpb.iphy.ac.cn; http://iopscience.iop.org/cpb

What follows is a list of articles you may be interested in

Simulations of hot electron transport in radiation-ablated plasma

Bin Zhao(赵斌), Tao Tao(陶骏), Rui Yan(闫锐), and Jian Zheng(郑坚)
Chin. Phys. B, 2023, 32 (**8**): 085201. DOI: 10.1088/1674-1056/acc0f3

Features of transport induced by ion-driven trapped-electron modes in tokamak plasmas

Hui Li(李慧), Ji-Quan Li(李继全), Feng Wang(王丰), Qi-Bin Luan(栾其斌),Hong-En Sun(孙宏恩), and Zheng-Xiong Wang(王正汹)
Chin. Phys. B, 2023, 32 (**7**): 075206. DOI: 10.1088/1674-1056/acae7e

Nonlinear mixing-based terahertz emission in inclined rippled density plasmas

K Gopal, A P Singh, and S Divya
Chin. Phys. B, 2023, 32 (**6**): 065202. DOI: 10.1088/1674-1056/aca9c9

Discrete Alfvén eigenmodes in the CFETR steady-state scenario

Yuan-Dan Lan(兰源丹), Shuang-Hui Hu(胡双辉), Si-Jie Ouyang(欧阳思杰),Wan-Po Zhu(朱万坡), and Xuan-Ge Huang(黄旋格)
Chin. Phys. B, 2023, 32 (**5**): 055201. DOI: 10.1088/1674-1056/aca397

Linear analysis of plasma pressure-driven mode in reversed shear cylindrical tokamak plasmas

Ding-Zong Zhang(张定宗), Xu-Ming Feng(冯旭铭), Jun Ma(马骏), Wen-Feng Guo(郭文峰), Yan-Qing Huang(黄艳清), and Hong-Bo Liu(刘洪波)
Chin. Phys. B, 2023, 32 (**1**): 015201. DOI: 10.1088/1674-1056/ac70b4

Global simulation of plasma series resonance effect in radio frequency capacitively coupled Ar/O_2 plasma

Xue Bai(白雪), Hai-Wen Xu(徐海文), Chong-Biao Tian(田崇彪),
Wan Dong(董婉), Yuan-Hong Song(宋远红)†, and You-Nian Wang(王友年)

Key Laboratory of Materials Modification by Laser, Ion, and Electron Beams (Ministry of Education), School of Physics, Dalian University of Technology, Dalian 116024, *China*

(Received 26 April 2023; revised manuscript received 26 June 2023; accepted manuscript online 5 July 2023)

Radio frequency capacitively coupled plasmas (RF CCPs) play a pivotal role in various applications in etching and deposition processes on a microscopic scale in semiconductor manufacturing. In the discharge process, the plasma series resonance (PSR) effect is easily observed in electrically asymmetric and geometrically asymmetric discharges, which could largely influence the power absorption, ionization rate, *etc*. In this work, the PSR effect arising from geometrically and electrically asymmetric discharge in argon–oxygen mixture gas is mainly investigated by using a plasma equivalent circuit model coupled with a global model. At relatively low pressures, as Ar content (α) increases, the inductance of the bulk is weakened, which leads to a more obvious PSR phenomenon and a higher resonance frequency ($\omega_{\rm psr}$). When the Ar content is fixed, varying the pressure and gap distance could also have different effects on the PSR effect. With the increase of the pressure, the PSR frequency shifts towards the higher order, but in the case of much higher pressure, the PSR oscillation would be strongly damped by frequent electron–neutral collisions. With the increase of the gap distance, the PSR frequency becomes lower. In addition, electrically asymmetric waveforms applied to a geometrically asymmetric chamber may weaken or enhance the asymmetry of the discharge and regulate the PSR effect. In this work, the Ar/O_2 electronegative mixture gas is introduced in a capacitive discharge to study the PSR effect under geometric asymmetry effect and electrical asymmetry effect, which can provide necessary guidance in laboratory research and current applications.

Keywords: capacitively coupled Ar/O_2 plasma, PSR effect, plasma equivalent circuit model, global model

PACS: 52.65.–y, 52.65.Ww, 52.80.Pi, 52.80.Tn **DOI:** 10.1088/1674-1056/ace427

1. Introduction

Radio frequency capacitively coupled plasmas (RF CCPs) have been widely used in plasma etching and deposition[1–4] in microelectronics industry in the last decades, because of their simple geometry and large-area processing structure with chemically active species, radicals, and energetical ions. The capacitively coupled plasmas (CCPs) are often geometrically asymmetric, and have unequal surface areas of the driving electrodes and grounded electrodes, especially when considering that the grounded surface usually includes the chamber wall. The geometric asymmetry effect (GAE) can significantly affect the power absorption dynamics and the distributions of charged particles, and thus influencing the quality and efficiency of etching or deposition. Moreover, for the electrical asymmetry effect (EAE), it was first proposed by driving a fundamental frequency and its second harmonic in a geometrically symmetric chamber,[5] and then was extended by applying peaks/valleys, sawtooth-up/-down, or Gaussian-type driving voltage waveforms even in geometrically asymmetric CCPs,[6,7] to have higher possibility of controlling not only ion properties but also electron power absorption and plasma density. At low-pressure CCPs, the RF sheath exhibits a similar charge–voltage characteristic of strong nonlinearity to an capacitance, while the bulk plasma has inductive and resistive properties, when taking into account the electron inertia and the power dissipation caused by collisions of electrons with neutrals and momentum transfer from the oscillating sheath edge, respectively.[8] The resonance between the two capacitive sheaths and the inductive bulk plasma comes into play owing to the GAE or EAE, and excites high harmonics of the discharge current,[9,10] which will affect the electron power absorption during rapid sheath expansion and generate multiple high-energy electron beams. In addition, the harmonics generated by the nonlinear PSR can significantly affect the local characteristics (electron or ion energy distribution) and the plasma uniformity.[11]

In recent years, particle-in-cell (PIC) simulations and electrical circuit models have been widely used to study the PSR effect. Donkó *et al.*[12] demonstrated by PIC simulations that high-frequency PSR oscillation can be excited in a geometrically symmetric discharge if the driving voltage waveform makes the discharge electrically asymmetric. Mussenbrock *et al.*[13] and Lieberman *et al.*[14] used a plasma equivalent circuit model and found that under geometrically asymmetric conditions, the nonlinear interaction between the plasma bulk and sheath will bring about the PSR effect and excite several harmonics of the fundamental frequency. In turn, the self-excitation of the PSR effect will enhance the electron heating mechanism in low pressure CCPs. In addition, using a plasma equivalent circuit model, Hei *et al.*[5] and Bora *et*

†Corresponding author. E-mail: songyh@dlut.edu.cn

© 2023 Chinese Physical Society and IOP Publishing Ltd

al.[9] found that although the chamber structure is symmetric, the electrically asymmetric waveforms applied to the driving electrode will also excite the high-order harmonics of voltage and current, and thus significantly changing the plasma heating process. They also found that the PSR effect can be suppressed or enhanced by changing the phase angle of the electrically asymmetric waveforms. But, in their work, the electron density and temperature, as input values to the equivalent circuit model, are fixed. To achieve a more self-consistent study, Schmidt *et al.*[15,16] used an equivalent circuit/global model, by taking into consideration an external electric circuit composed of lumped elements in their study of capacitive Ar discharge, in which the plasma density and electron temperature are obtained somewhat self-consistently. Compared with the equivalent circuit and PIC/MCC models, the circuit/global model achieves a very self-consistent study and saves computational costs, which is beneficial to the understanding of the observed PSR phenomenon.

Most of previous studies mentioned above focused on Ar plasmas, but in many plasma applications, especially in etching and deposition processes, electronegative gases or reactive mixture gases are more widely used. For example, Xu *et al*. deposited SiO_2 films in their SiH_4/N_2O discharges experiment.[17] Generally, gas properties can significantly affect the space–time dynamics of the high-energy electrons, ion flux/energy distribution function, and plasma heating mechanism.[18] Rare gas Ar is often used as the dilution gas in electronegative gases. Capacitively coupled Ar/O_2 discharge possesses essential advantages in the sputtering deposition of aluminum, etch photoresist and polymer films, tungsten, high-temperature superconducting films, and growth of silica dielectric films.[19,20] Gudmundsson and Thorsteinsson[21] found that the electron density decreases with the augment of volume ratio of O_2 molecule in their global studies of dissociation processes in a low-pressure high-density Ar/O_2 discharge. They observed a growing electronegativity and attributed it to the intensification of the negative ion generation source, such as the dissociative electron attachment to O_2. Hong *et al.*[22] also found that the addition of electronegative O_2 reduces the electron density and increases the electronegativity in their capacitive Ar/O_2 experiments. However, the PSR effect in Ar/O_2 mixture plasmas has not yet been understood very clearly. Therefore, corresponding research efforts are of great significance.

In this work, the PSR effect in an Ar/O_2 mixture plasma caused by geometrical and electrical asymmetry is investigated, based on an equivalent circuit/global model. The rest of this paper is organized as follows. The simulation methods are described in Section 2, while the simulation results are presented and discussed in Section 3. A short summary is given in Section 4.

2. Methods

The schematic diagram of the plasma equivalent circuit model used in this study is shown in Fig. 1, in which the plasma may be equivalently regarded as a series of LCR elements, in order to provide explicit explanations for the PSR effect. As indicated in previous studies,[15,23] the RF sheath is modeled as a parallel connection of a constant current source, a diode, and a nonlinear capacitor. For the driving sheath, the ion current flowing onto the surface is described as $I_{\mathrm{i,d}} = eA_{\mathrm{d}}n_{\mathrm{i}}u_{\mathrm{B}}$, with the driving electrode areas A_{d}, the positive ion density n_{i} and the Bohm speed u_{B}. Assuming that the electrons obey a Boltzmann distribution in the sheath, the electron current can then be expressed as $I_{\mathrm{e,d}} = eA_{\mathrm{d}}n_{\mathrm{e}}\bar{v}_{\mathrm{e}}\,\mathrm{e}^{-eV_{\mathrm{s,d}}/k_{\mathrm{B}}T_{\mathrm{e}}}$, in which n_{e} is the electron density, $\bar{v}_{\mathrm{e}}$ is the mean thermal speed of the electron, $V_{\mathrm{s,d}}$ is the driving sheath voltage, T_{e} is the electron temperature, and k_{B} is the Boltzmann constant. Meanwhile, according to the homogeneous model of Liberman,[14,15] the sheath capacitance is modeled as a nonlinear capacitor $C_{\mathrm{s,d}} = (en_{\mathrm{i}}\varepsilon_0 A_{\mathrm{d}}^2/2V_{\mathrm{s,d}})^{1/2}$. Accordingly, for the grounded sheath, the ion current, the electron current, and the sheath capacitance can be expressed as $I_{\mathrm{i,g}} = eA_{\mathrm{g}}n_{\mathrm{i}}u_{\mathrm{B}}$, $I_{\mathrm{e,g}} = eA_{\mathrm{g}}n_{\mathrm{e}}\bar{v}_{\mathrm{e}}\,\mathrm{e}^{-eV_{\mathrm{s,g}}/k_{\mathrm{B}}T_{\mathrm{e}}}$, and $C_{\mathrm{s,g}} = (en_{\mathrm{i}}\varepsilon_0 A_{\mathrm{g}}^2/2V_{\mathrm{s,g}})^{1/2}$, respectively. Owing to the electron inertia and the electron power dissipation, the bulk plasma behaves like an inductance and a resistance, which can be represented as $L_{\mathrm{p}} = m_{\mathrm{e}}(L-l_{\mathrm{s}})/e^2 n_{\mathrm{e}}A_{\mathrm{d}}$ and $R_{\mathrm{p}} = \nu_{\mathrm{eff}}L_{\mathrm{p}}$, in which m_{e} is the electron mass, l_{s} is the sheath width, L is the electrode gap, and ν_{eff} is the effective collision frequency involving with the effect of ohmic and stochastic heating.[15,24] Therefore, the resonance frequency can be expressed as

$$\omega_{\mathrm{psr}} = \frac{1}{\sqrt{L_{\mathrm{p}}C_{\mathrm{s}}}} = \left(\frac{l_{\mathrm{s}}}{L-l_{\mathrm{s}}}\right)^{1/2}\omega_{\mathrm{pe}},$$

in which ω_{pe} is the electron plasma frequency. By applying the Kirchhoff's law to the model,[15,24] a set of four differential equations can be obtained, which describe the two sheath voltages, the DC self-bias, and the RF current, and the above-mentioned fundamental plasma parameters can be finally achieved.

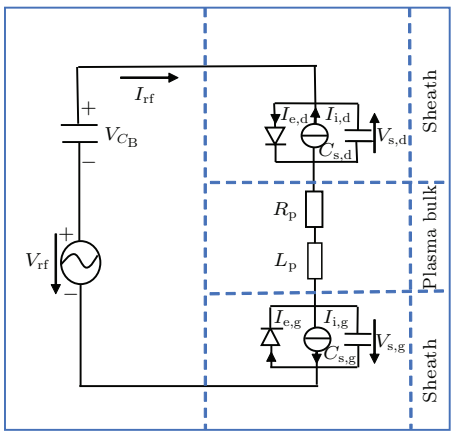


Fig. 1. Schematic picture of equivalent circuit network.

The global (volume-averaged) model in this paper is based on the model used by Schmidt *et al.*[15] and Liu *et al.*[25] Specific chemical reactions are shown in Table 1. In this table, only the important reactions of Ar/O_2 plasma are considered, and the reactions between ozone O_3 and negative O_2^-, and between ozone O_3 and O_3^- are ignored because O is dominant in the discharge compared with O_2^- and O_3^-.[25] The main charged particles, like Ar, Ar*, Ar^+, O_2, O_2^*, O_3, O, O*, O_2^+, O^+, O^-, and e, are traced in this work.

A flowchart of the simulation is shown in Fig. 2. First, the estimated values of all circuit elements are given for a transient simulation of the entire system of interest. Then, a transient simulation of the circuit determines all currents and voltages at each branch and node. Therefore, the absorbed power of the plasma and the averaged voltages across the sheaths can be calculated from the circuit model (see Fig. 1). The global model is then used to calculate the electron density, ion density, and electron temperature from these values, and the elements of the plasma model can be updated to obtain new values of all the circuit elements in Fig. 1. Thus, the simulation is iterated until a steady state of the particle density and power has been reached. At this stage, for a specific circuit, the consistent values of the electron and ion density, the plasma absorbed power, and any other current, voltage, or power of interest are obtained.

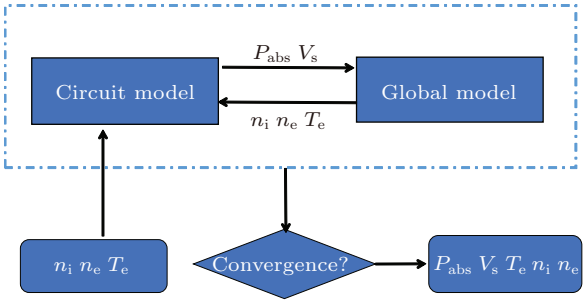


Fig. 2. Algorithm flowchart of simulation.

Table 1. Chemical reactions considered in global model.

No.	Reaction	Rate coefficient ($m^3 \cdot s^{-1}$)	Threshold (eV)	References
1	$e + Ar \rightarrow e + Ar$	A[a]	$3m_eT_e/M$[b]	[25]
2	$e + Ar \rightarrow e + Ar^*$	$9.73\times10^{-16}\times T_e^{-0.07}\times\exp(-11.69/T_e)$	11.56	[25]
3	$e + Ar \rightarrow Ar^+ + 2e$	$2.39\times10^{-14}\times T_e^{0.57}\times\exp(-17.43/T_e)$	15.76	[25]
4	$e + Ar^* \rightarrow Ar^+ + 2e$	$2.05\times10^{-13}\times\exp(-4.95/T_e)$	4.43	[25]
5	$e + Ar^* \rightarrow Ar + e$	2.0×10^{-13}	11.56	[25]
6	$Ar^* + Ar^* \rightarrow Ar + Ar^+ + e$	6.2×10^{-16}		[25]
7	$e + O_2 \rightarrow e + O_2$	$\exp\left(\begin{array}{l}-30.7683+0.3531\times\ln(T_e)\\+0.2068\times(\ln(T_e))^2-0.0406\times(\ln(T_e))^3\end{array}\right)$	$3m_eT_e/M$	[25]
8	$e + O_2 \rightarrow O + O + e$	$4.23\times10^{-15}\times\exp(-5.56/T_e)$	6.0	[25]
9	$e + O_2 \rightarrow O + O^* + e$	$5.0\times10^{-14}\times\exp(-8.4/T_e)$	8.4	[25]
10	$e + O_2 \rightarrow O + O^-$	$1.07\times10^{-15}\times T_e^{-1.39}\times\exp(-6.26/T_e)$	4.2	[25]
11	$e + O_2 \rightarrow O_2^+ + 2e$	$2.34\times10^{-15}\times T_e^{1.03}\times\exp(-12.9/T_e)$	12.06	[25]
12	$e + O \rightarrow O + e$	$\exp\left(\begin{array}{l}-30.9463+0.9484\times\ln(T_e)\\-0.14158\times(\ln(T_e))^2-0.0154\times(\ln(T_e))^3\end{array}\right)$	$3m_eT_e/M$	[25]
13	$e + O \rightarrow O^* + e$	$4.47\times10^{-15}\times\exp(-2.286/T_e)$	1.96	[25]
14	$e + O \rightarrow O^+ + 2e$	$9.0\times10^{-15}\times T_e^{0.7}\times\exp(-13.6/T_e)$	13.61	[25]
15	$e + O^* \rightarrow O^+ + 2e$	$9.0\times10^{-15}\times T_e^{0.7}\times\exp(-11.6/T_e)$	11.6	[25]
16	$e + O^- \rightarrow O + 2e$	$1.73\times10^{-13}\times\exp(-5.76/T_e+7.3/T_e^2-3.84/T_e^3)$		[25]
17	$O_2 + O^* \rightarrow O + O_2$	4.1×10^{-17}		[25]
18	$O + O^* \rightarrow O + O$	8.1×10^{-18}		[25]
19	$O_2^+ + O^- \rightarrow O_2 + O$	$1.5\times10^{-13}\times(300/T_g)^{0.5}$		[25]
20	$O^+ + O^- \rightarrow O + O$	$2.7\times10^{-13}\times(300/T_g)^{0.5}$		[25]
21	$O_2^+ + e \rightarrow O^* + O$	$2.2\times10^{-14}\times(T_e)^{-0.5}$		[25]
22	$e + O_2 \rightarrow O_2^* + e$	$1.7\times10^{-15}\times\exp(-3.1/T_e)$	0.98	[25]
23	$e + O_2^* \rightarrow O + O^-$	$2.28\times10^{-16}\times\exp(-2.29/T_e)$	3.22	[25]
24	$e + O_2^* \rightarrow O_2^+ + 2e$	$9.0\times10^{-16}\times\exp(-11.6/T_e)$	11.08	[25]
25	$e + O_2^* \rightarrow 2O + e$	$4.2\times10^{-15}\times\exp(-4.6/T_e)$	5.023	[25]
26	$e + O_2^* \rightarrow O_2 + e$	$5.6\times10^{-15}\times\exp(-2.2/T_e)$	0.98	[25]
27	$O + O^- \rightarrow O_2 + e$	1.4×10^{-16}		[25]
28	$O^- + O_2^* \rightarrow O_3 + e$	1.0×10^{-16}		[25]
29	$e + O_3 \rightarrow O_2 + O + e$	1.4×10^{-14}	6.0	[25]
30	$e + O_3 \rightarrow O_2 + O^-$	$2.12\times10^{-15}\times\exp(-0.93/T_e)$	4.2	[25]
31	$O_2 + Ar^* \rightarrow O_2 + Ar$	1.12×10^{-15}		[25]
32	$O_2 + Ar^+ \rightarrow O_2^+ + Ar$	1.2×10^{-17}		[25]
33	$O_2 + Ar^* \rightarrow O + O + Ar$	5.8×10^{-17}		[25]
34	$O + Ar^* \rightarrow O + Ar$	8.1×10^{-18}		[25]
35	$O + Ar^+ \rightarrow O^+ + Ar$	1.21×10^{-17}		[25]
36	$O^- + Ar^+ \rightarrow O + Ar$	2.7×10^{-13}		[25]

[a] Letter A refers to that the coefficient is the integral of electron impact cross sections under Maxwellian distribution.
[b] T_e denotes the electron temperature, m_e the mass of the electron, and M the mass of the ion.

3. Result and discussion

Before running the code to simulate the capacitively coupled Ar/O_2 discharge, a number of tests are conducted to repeat some of the results in Ref. [26] and the test results are in good agreement with the results in the literature. Generally, the side walls of the discharge chamber are usually grounded, resulting in a geometrically asymmetric discharge chamber with different driving and grounded electrode areas. Therefore, to more closely match the laboratory discharge with geometry asymmetry, firstly in the following discussion, a normal RF input voltage $V = 100\cos(2\pi ft)$ is applied, where $f = 13.56$ MHz (see Fig. 3(c)). We explore the Ar content on the PSR effect excited by the geometrically asymmetric discharges, with the gap distance $L = 3$ cm and pressure $p = 15$ mTorr (1 Torr = 1.33322×10^2 Pa), while the driving and grounded electrode areas are 100 cm^2 and 300 cm^2, respectively.

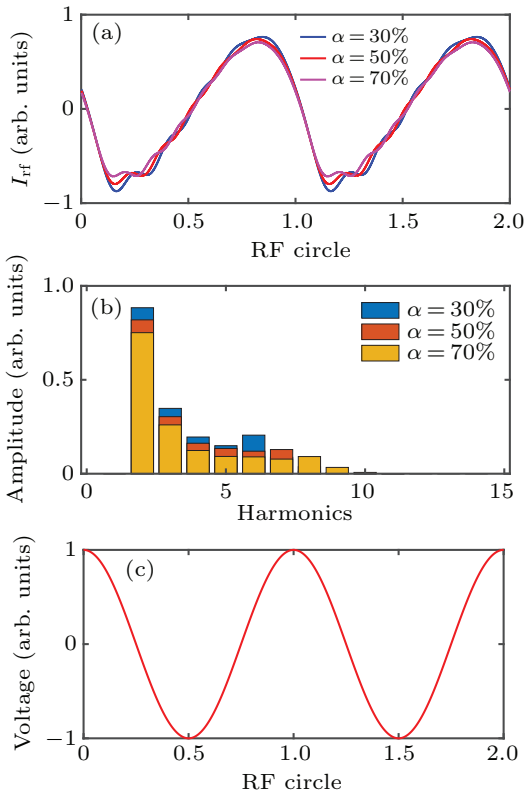


Fig. 3. Time evolution of (a) plasma current and (b) its fast Fourier transform (FFT) analysis (the fundamental frequency is not included in this plot) at different values of Ar content α, and (c) sinusoidal voltage waveform, under discharge conditions: $V = 100\cos(2\pi ft)$, $L = 3$ cm, $A_d = 100$ cm^2, $A_g = 300$ cm^2, and $p = 15$ mTorr.

As expected, the distortions of the current are mainly due to the generation of the PSR effect, as shown in Fig. 3. In the cases of $\alpha = 30\%$, 50%, and 70%, ω_{psr} is $6\omega_{rf}$, $7\omega_{rf}$, and $8\omega_{rf}$, corresponding to the 6th, 7th, and 8th harmonics of the current, suggesting that the PSR frequency $\omega_{psr} = 1/\sqrt{L_pC_s}$ gradually shifts towards the higher order in the discharge with more electropositive Ar and less electronegative O_2 in the discharge. Actually, with the increase of the Ar content, as shown in Fig. 4, the electron density increases monotonically, leading to the monotonical decrease of the bulk inductance, while the effects of the Ar content on the sheath capacitance can be approximately neglected, resulting in the increase of the PSR frequency. Thus, in an electropositive discharge, the PSR frequency becomes larger than that in an electronegativity discharge.

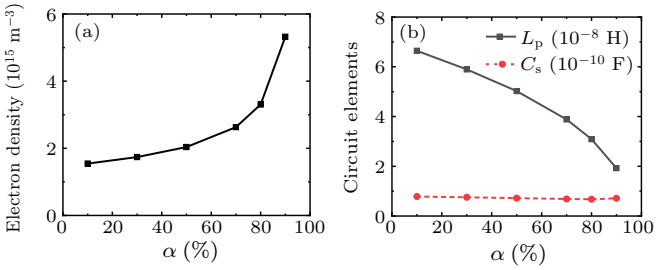


Fig. 4. Variations of (a) electron density, (b) bulk inductance L_p and sheath capacitance C_s with Ar content α under the same discharge conditions as those in Fig. 3.

In addition, figure 5 shows the harmonic amplitudes of the plasma current at pressures of 4 mTorr, 15 mTorr, and 60 mTorr, respectively, with $\alpha = 30\%$, 50%, and 70%. It is easily seen that in the case of lower pressure, ω_{psr} gradually shifts towards the higher order with the pressure increasing owing to the increased electron density in a relatively electropositive discharge, except the case of $\alpha = 30\%$. When Ar content is $\alpha = 30\%$ with the discharge more electronegative, ω_{psr} is observed at $6\omega_{rf}$ at pressures of 4 mTorr and 15 mTorr, suggesting that the PSR effect becomes weaker in an electronegativity discharge, and the FFT analyses do not show the variations of the resonance frequency with pressure clearly. At higher pressure of about 60 mTorr, these series resonances are all strongly damped by the more frequent collisions of electrons with the neutral particles in the background, so the PSR frequency can hardly be calculated and the PSR effect cannot be observed.

For different gap distances, it can be observed from Fig. 6 that for each of argon content $\alpha = 30\%$, 50%, and 70%, the degree of RF plasma current distortion mainly depends on the gap distance. The FFT analyses, which are conducted to obtain the harmonic components of the plasma current in Fig. 6 show that in each of the cases of $L = 3$ cm, 4 cm, and 7 cm, the PSR frequency gradually shifts towards the lower order with the increase of gap distance at fixed Ar content, specifically, for $\alpha = 30\%$ it shifts from $6\omega_{rf}$ to $4\omega_{rf}$, for $\alpha = 50\%$ from $7\omega_{rf}$ to $5\omega_{rf}$, and for $\alpha = 70\%$, ω_{psr} corresponds to the 8th, 7th, and 6th harmonics of the current. As shown in Fig. 7, with the increase of the gap distance, the inductance and the power deposition of the plasma are significantly enhanced because of larger valid discharge space, leading to the decrease of ω_{psr}, while the effect of the gap distance increase on the sheath capacitance is negligible.

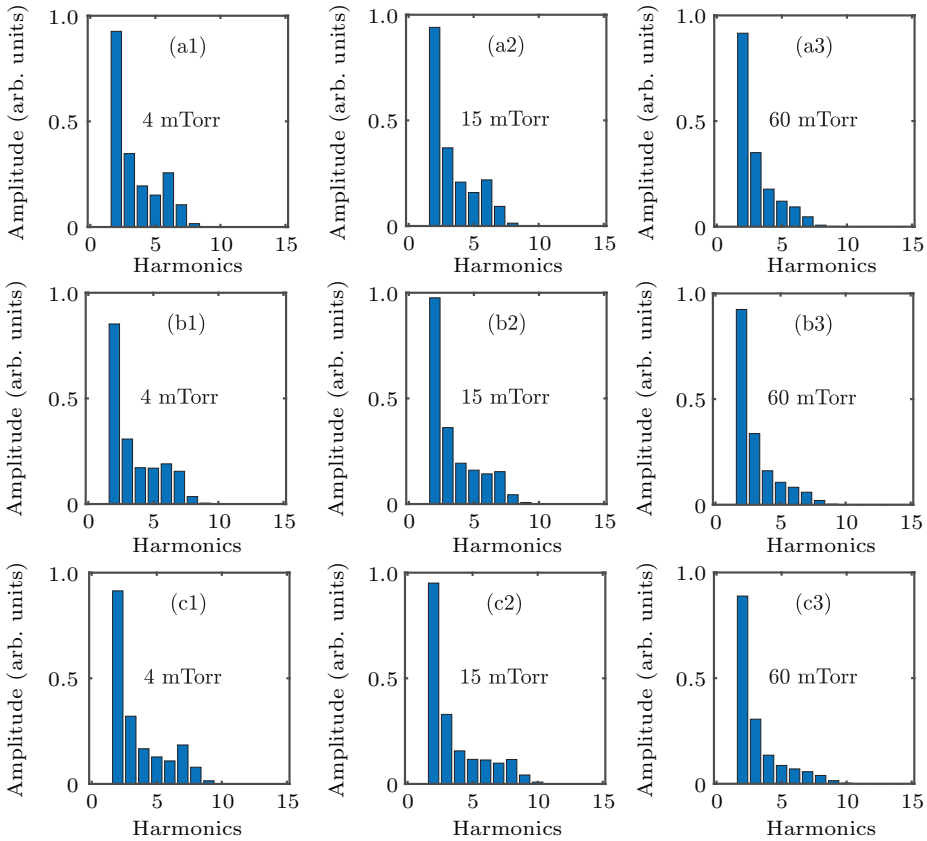


Fig. 5. FFTs of plasma current (the fundamental frequency is not included in this plot) at (a1) 4 mTorr and $\alpha = 30\%$, (a2) 15 mTorr and $\alpha = 30\%$, (a3) 60 mTorr and $\alpha = 30\%$, (b1) 4 mTorr and $\alpha = 50\%$, (b2) 15 mTorr and $\alpha = 50\%$, (b3) 60 mTorr and $\alpha = 50\%$, (c1) 4 mTorr and $\alpha = 70\%$, (c2) 15 mTorr and $\alpha = 70\%$, (c3) 60 mTorr and $\alpha = 70\%$, with discharge conditions: RF voltage waveform $V = 100\cos(2\pi ft)$, $A_d = 100$ cm^2, $A_g = 300$ cm^2, and $L = 3$ cm.

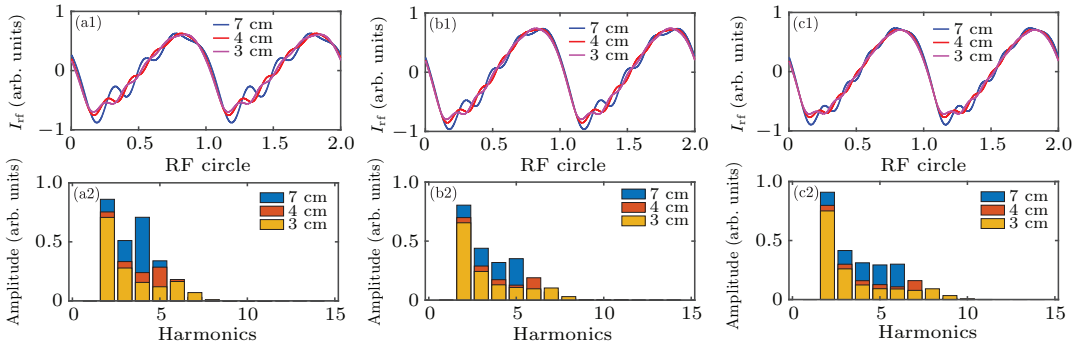


Fig. 6. Time evolution of plasma current and its FFT analysis (with no fundamental frequency included in this plot) at three different gap distances (3 cm, 4 cm, and 7 cm) and $\alpha = 30\%$ (a), 50% (b), and 70% (c), with discharge conditions: RF voltage waveform identical to that in Fig. 3(c), $A_d = 100$ cm^2, $A_g = 300$ cm^2, and $p = 15$ mTorr.

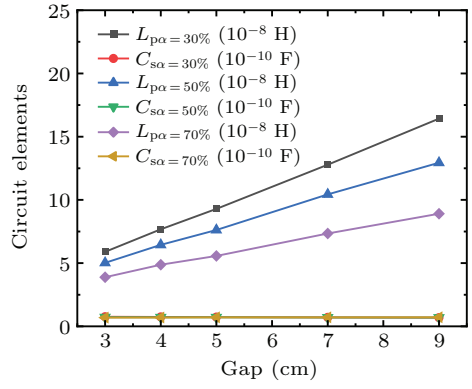


Fig. 7. Variations of ciucuit elements (bulk inductance L_p and sheath capacitance C_s) with gap distance, under the same discharge conditions as those in Fig. 6.

As is well known, the EAE is introduced for realizing the separate control of the mean ion energy and flux at the electrodes in radio-frequency capacitive discharges with identical electrode areas driven, while the PSR effect is also expected to be observed. To clarify more details of the PSR effect excited by electrically asymmetric waveforms in a geometrically symmetric chamber in the following discussion, the voltage waveform applied is adopted as a Gaussian-type voltage $V = V_0 \exp(-\beta(t - t_0))$ with a repetition frequency of 13.56 MHz (see Fig. 8(c)), where V_0 is the voltage amplitude, t_0 is the time of the pulse maximum, and $\Delta\tau = 2\sqrt{\ln 2/\beta}$ is the full width at half-maximum of the Gaussian-type voltage

waveform.

First of all, our model has been verified by the following simulation results to some extent, which lays a foundation for further studying the physical mechanisms. For the discharge conditions presented here, the voltage amplitude is $V_0 = 250$ V, pulse width $\Delta\tau = 5$ ns, gap distance $L = 2$ cm, pressure $p = 35$ mTorr, and Ar content $\alpha = 25\%$. And the driving area and the grounded electrode area are both 400 cm^2 in the circuit/global model. Based on the equivalent circuit/global model and the PIC/MCC model, the time evolution of the plasma current and its FFTs are shown in Figs. 8(a) and 8(b), in which it can be easily seen that the plasma current density presents an evident PSR oscillation under an applied Gaussian-type voltage waveform. The FFTs show that there exist high-order harmonics in the current waveform, which further indicates that there is PSR in this geometrically symmetric CCP. Since the Gaussian-type voltage with a pulse width of 5 ns exhibits a similar behavior to the waveform composed of 10 harmonics, it is easily approximated that the first 10 harmonic components are dominantly generated by the fundamental Gaussian frequency, while the other higher harmonic components are excited by the PSR effect due to the EAE.[27] In both models, we see a significant harmonic content for the current density, with the largest harmonics at 16, which corresponds to the resonance frequency ω_{psr}.

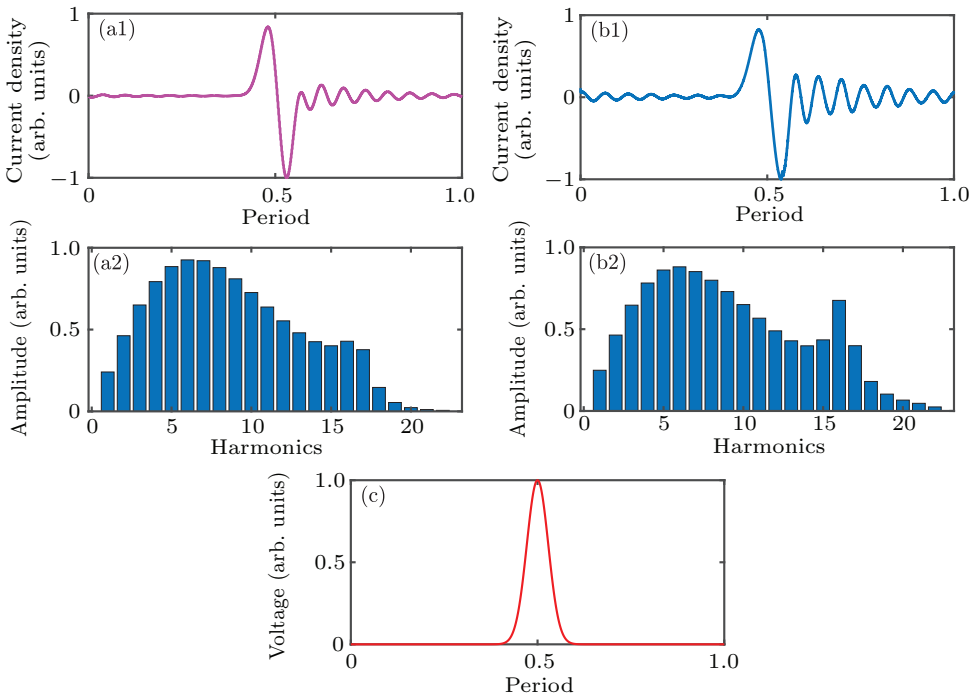


Fig. 8. Time evolution of current density and its FFT analysis obtained from (a) circuit/global model and (b) PIC/MCC model, and (c) Gaussian-type voltage waveform under discharge conditions: $\Delta\tau = 5$ ns, $L = 2$ cm, $p = 35$ mTorr, and $\alpha = 25\%$.

We also explored the effect of Ar content α on PSR, which is excited by the Gaussian-type voltage waveform in a geometrically symmetric chamber. As shown in Fig. 9, in the cases of $\alpha = 30\%$, 50%, and 70%, the values of PSR frequency ω_{psr} are $13\omega_{rf}$, $15\omega_{rf}$, and $17\omega_{rf}$, respectively. Like the scenario of geometric asymmetry, in a relatively electropositive discharge, the PSR frequency becomes larger than that in a more electronegative discharge, which is also because the electron density increases and the bulk inductance decreases (see Fig. 10). However, it is also important to note that, in this Gaussian-type voltage driven discharge, the PSR frequency becomes larger than that in the geometrically asymmetric discharge, with the plasma current oscillating violently (see Figs. 3(a) and 9(a)).

The coupling of the EAE and GAE and its effect on the PSR effect are also interesting and worth investigating, in this Ar/O_2 capacitive discharge. In the following, by driving and modulating the Gaussian-type voltage waveform with positive amplitude and negative amplitude, the PSR effect will be studied in a geometrically asymmetric discharge with $A_d < A_g$, in which the driving electrode area A_d is varied to modulate the geometrical asymmetry of the discharge.

As shown in Fig. 11, the extent of the plasma current distortion mainly depends on the driving electrode area. With the Gaussian waveform $V = 250\exp(-\beta(t-t_0))$ driven here, values of ω_{psr} are easily observed to be $14\omega_{rf}$, $15\omega_{rf}$, and $16\omega_{rf}$ in the cases of $A_d = 400$ cm^2, 300 cm^2, and 200 cm^2, respectively. So, ω_{psr} gradually shifts towards the higher order with the increase of geometric asymmetry extent. Thus, with the superposition effects of the increasing difference between the

two electrode areas and the Gaussian waveform with a positive amplitude, the asymmetry of the discharge increases with the formation of a higher negative DC self bias. Wang *et al.*[7] found from their particle simulation results that a thicker sheath would be formed at the powered electrode due to the strong negative DC self-bias, which can lead to fast sheath expansion and excitation of strong PSR oscillations. From our results, with the enhancement of the superposition of electrical and geometrical asymmetry, the absolute value of the negative DC self-bias voltage really becomes larger, as shown in Fig. 12(a), which can result in the excitation of stronger PSR oscillation and the increase of $\omega_{\rm psr}$. In this case, the significant decrease of the sheath capacitance with the driving electrode area lessening plays a major role in determining the PSR frequency shift, compared with that of the bulk inductance as shown in Fig. 12(b). To further understand the PSR effect by imposing both EAE and GAE, we now set the voltage source amplitude to -200 V, but keep other discharge parameters unchanged. As shown in Fig. 13, by changing the sign of the applied voltage amplitude, the capacitive plasma still keeps asymmetric with high-order harmonics observed in the plasma current waveform, but the PSR frequency $\omega_{\rm psr}$ gradually shifts towards the lower order with the decrease of the driving electrode area, specifically, from $13\omega_{\rm rf}$ to $10\omega_{\rm rf}$.

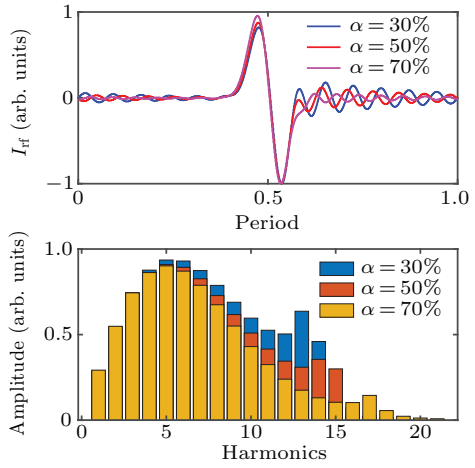


Fig. 9. (a) Time evolution of plasma current and (b) its FFT analysis at different values of Ar content α under discharge conditions: Gaussian-type voltage waveform $V = 250\exp(-\beta(t-t_0))$, $\Delta\tau = 6$ ns, $L = 3$ cm, $A_{\rm d} = A_{\rm g} = 400$ cm^2, and $p = 15$ mTorr.

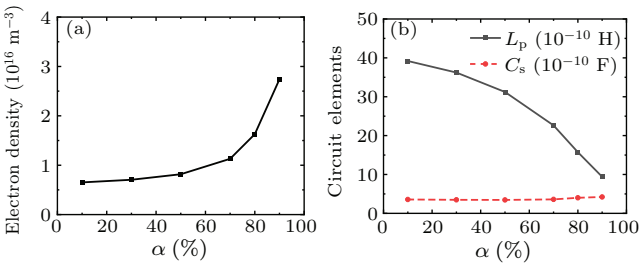


Fig. 10. (a) Electron density versus Ar content α and (b) bulk inductance $L_{\rm p}$ and sheath capacitance $C_{\rm s}$ versus Ar content α, under the same discharge conditions as those in Fig. 9.

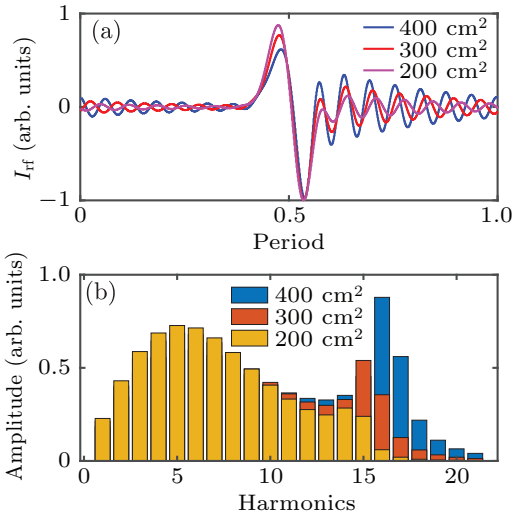


Fig. 11. (a) Time evolution of plasma current and (b) its FFT analysis, for different values of driving electrode area $A_{\rm d}$ under discharge conditions: Gaussian-type voltage waveform $V = 250\exp(-\beta(t-t_0))$, $\Delta\tau = 6$ ns, $L = 3$ cm, $A_{\rm g} = 400$ cm^2, $p = 15$ mTorr, and Ar content $\alpha = 50\%$.

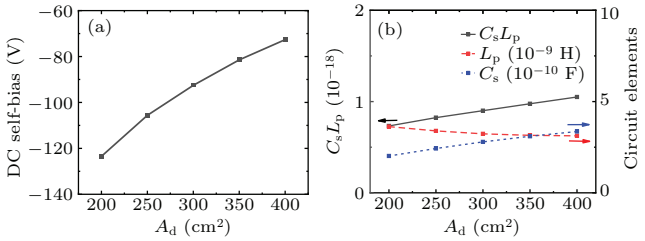


Fig. 12. (a) DC self-bias versus $A_{\rm d}$, and (b) bulk inductance $L_{\rm p}$, sheath capacitance $C_{\rm s}$, and $C_{\rm s}L_{\rm p}$ versus $A_{\rm d}$, under the same discharge conditions as those in Fig. 11.

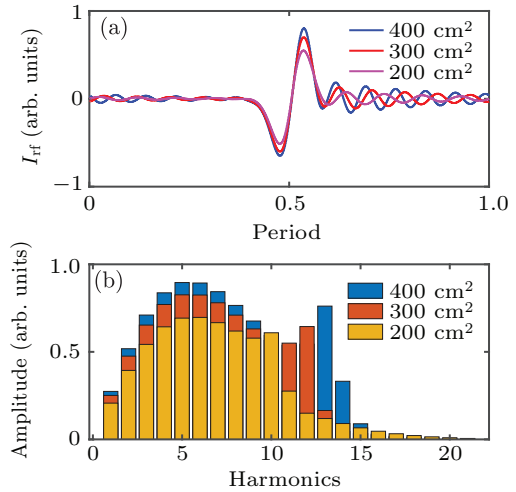


Fig. 13. (a) Time evolution of plasma current and (b) its FFT analysis, for different values of driving electrode area $A_{\rm d}$, under discharge conditions: Gaussian-type voltage waveform $V = -200\exp(-\beta(t-t_0))$, $\Delta\tau = 6$ ns, $L = 3$ cm, $A_{\rm g} = 400$ cm^2, $p = 15$ mTorr, and Ar content $\alpha = 50\%$.

As shown in Fig. 14(a), owing to the destructive superposition between the electrical asymmetry and geometrical asymmetry, the DC self bias is positive[7] and decreases as $A_{\rm d}$ decreases, so the sheath becomes thinner and expands slowly, leading to the weakening of PSR oscillation and the decreasing of the resonance frequency. Figure 14(b) shows that with the decrease of the driving electrode area, the sheath capacitance lessens very slightly, but the bulk inductance increases

a lot and gradually becomes the main reason for the resonance frequency decreasing, while the electrical asymmetry and geometrical asymmetry suppress each other. Therefore, we demonstrate that by tuning the positive amplitude and negative amplitude of the Gaussian-type voltage waveform, the asymmetry generated by the reactor geometry can be enhanced or suppressed by the electrical asymmetry.

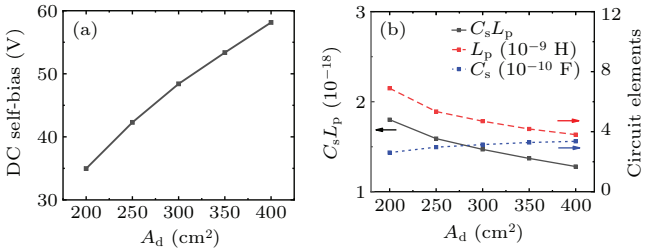


Fig. 14. (a) DC self-bias versus A_d, and (b) bulk inductance L_p, sheath capacitance C_s, and C_sL_p versus A_d under the same discharge conditions as those in Fig. 13.

4. Conclusions

In the present work, we have studied the PSR effect of a CCP in Ar/O_2 mixed gas, under EAE and GAE, based on a plasma equivalent circuit/global model. By varying the Ar content α and the gap distance, the bulk inductance mainly determines the variation of resonance frequency. The PSR frequency gradually shifts towards the higher order in more electropositive Ar and less electronegative O_2 owing to the decrease of the bulk inductance. And because of the larger effective discharge space, the bulk inductance is significantly enhanced by increasing the gap distance, resulting in the decrease of ω_{psr}. It is also observed that the resonance frequency gradually shifts towards the higher order, which is attributed to the significant enhancement of the electron density with the increase of the pressure. And meanwhile, the PSR oscillation can be strongly damped by the electron–neutral collisions at higher pressure. In addition, the geometrical asymmetry can be enhanced or suppressed by tuning the positive amplitude or negative amplitude of the Gaussian-type voltage waveform, respectively. We believe that regarding the Ar/O_2 capacitive discharge, specifically, the influence of Ar content on the plasma absorb power and heating mechanisms, there remains much room to be explored.

Acknowledgement

Project supported by the National Natural Science Foundation of China (Grant Nos. 12020101005 and 11975067).

References

[1] Chu P K, Chen J Y, Wang L P and Huang N 2002 *Mater. Sci. Eng. R Reports* **36** 143
[2] Ostrikov K 2005 *Rev. Mod. Phys.* **77** 489
[3] Wang L, Wen D Q, Tian C B, Song Y H and Wang Y N 2021 *Acta Phys. Sin.* **70** 095214 (in Chinese)
[4] Wu L C, Yin G Q, Meng X G, Zhou Y Y and Wang J J 2020 *Nucl. Fusion Plasma Phys.* **40** 372
[5] Heil B G, Czarnetzki U, Brinkmann R P and Mussenbrock T 2008 *J. Appl. Phys.* **41** 165202
[6] Lafleur T 2016 *Plasma Sources Sci. Technol.* **25** 013001
[7] Wang L, Hartmann P, Donkó Z, Song Y H and Schulze J 2021 *Plasma Sources Sci. Technol.* **30** 054001
[8] Cao M, Lu Y, Cheng J and Ji L 2016 *Jpn. J. Appl. Phys.* **55** 096201
[9] Bora B, Bhuyan H, Favre M, Wyndham E and Wong C S 2013 *J. Appl. Phys.* **113** 153301
[10] Bora B, Soto L 2014 *Phys. Plasmas* **21** 083509
[11] Zhao K, Wen D Q, Liu Y X, Lieberman M A, Economou D J and Wang Y N 2019 *Phys. Rev. Lett.* **122** 185002
[12] Donkó Z, Schulze J, Czarnetzki U and Luggenhölscher D 2009 *Appl. Phys. Lett.* **94** 131501
[13] Mussenbrock T, Brinkmann R P, Lieberman M A, Lichtenberg A J and Kawamura E 2008 *Phys. Rev. Lett.* **101** 085004
[14] Lieberman M A, Lichtenberg A J, Kawamura E, Mussenbrock T and Brinkmann R P 2008 *Phys. Plasmas* **15** 063505
[15] Schmidt F, Mussenbrock T and Trieschmann J 2018 *Plasma Sources Sci. Technol.* **27** 105017
[16] Schmidt F, Schulze J, Johnson E, Booth J P, Keil D, French D M, Trieschmann J and Mussenbrock T 2019 *Plasma Sources Sci. Technol.* **27** 095012
[17] Xu Q, Li Y X, Li X N, Wang J B, Yang F and Yang Y 2017 *Mod. Phys. Lett. B* **31** 1750055
[18] Cao L Y, Ma X P, Deng L L, Lu M T and Xin Y 2021 *Acta Phys. Sin.* **70** 115204 (in Chinese)
[19] Jiang X Z, Li W liang, Wumaier T and Yao H Bin 2019 *Chem. Phys. Lett.* **730** 472
[20] Babaeva N Y, Lee J K, Shon J W and Hudson E A 2005 *J. Vac. Sci. Technol. A.* **23** 699
[21] Gudmundsson J T and Thorsteinsson E G. 2007 *Plasma Sources Sci. Technol.* **16** 399
[22] Hong B S, Yuan T, Zou S, Tang Z H, Xu D S, Yu Y Q, Wang X S and Xin Y 2013 *Acta Phys. Sin.* **62** 115202 (in Chinese)
[23] Bora B 2015 *Plasma Sources Sci. Technol.* **24** 054002
[24] Bora B, Bhuyan H, Favre M, Wyndham E and Chuaqui H 2012 *Appl. Phys. Lett.* **100** 094103
[25] Liu W, Wen D Q, Zhao S X, Gao F and Wang Y N 2015 *Plasma Sources Sci. Technol.* **24** 025035
[26] Lafleur T, Chabert P and Booth J P 2014 *Plasma Sources Sci. Technol.* **23** 035010
[27] Lafleur T and Booth J P 2012 *J. Phys. D: Appl. Phys.* **45** 395203